A perfect X-ray beam splitter and its applications to time-domain interferometry and quantum optics exploiting free-electron lasers

Sven Reiche[a], Gregor Knopp[a], Bill Pedrini[a], Eduard Prat[a], Gabriel Aeppli[a,b,c,d,1], and Simon Gerber[a,1]

[a]Large Research Facilities and Photon Science Divisions, Paul Scherrer Institut, CH-5232 Villigen PSI, Switzerland; [b]Department of Physics, Eidgenössische Technische Hochschule Zurich, CH-8093 Zurich, Switzerland; [c]Institut de Physique, École Polytechnique Fédérale Lausanne, CH-1015 Lausanne, Switzerland; and [d]Quantum Center, Eidgenössische Technische Hochschule Zurich, CH-8093 Zurich, Switzerland

Contributed by Gabriel Aeppli; received September 29, 2021; accepted December 30, 2021; reviewed by Jerome Hastings and Claudio Pellegrini

X-ray free-electron lasers (FELs) deliver ultrabright X-ray pulses, but not the sequences of phase-coherent pulses required for time-domain interferometry and control of quantum states. For conventional split-and-delay schemes to produce such sequences, the challenge stems from extreme stability requirements when splitting Ångstrom wavelength beams, where the tiniest path-length differences introduce phase jitter. We describe an FEL mode based on selective electron-bunch degradation and transverse beam shaping in the accelerator, combined with a self-seeded photon emission scheme. Instead of splitting the photon pulses after their generation by the FEL, we split the electron bunch in the accelerator, prior to photon generation, to obtain phase-locked X-ray pulses with subfemtosecond duration. Time-domain interferometry becomes possible, enabling the concomitant program of classical and quantum optics experiments with X-rays. The scheme leads to scientific benefits of cutting-edge FELs with attosecond and/or high-repetition rate capabilities, ranging from the X-ray analog of Fourier transform infrared spectroscopy to damage-free measurements.

free-electron lasers | X-rays | nonlinear optics | phase coherence | spectroscopy

For a decade, ultrashort, intense, and coherent X-ray pulses for experiments in all fields of natural science have been delivered by X-ray free-electron lasers (FELs) (1). Missing are phase-locked pulses, i.e., pulse pairs with a fixed phase relation, which would allow full exploitation of the coherence properties and, thereby, extend coherent control schemes to shorter than optical and ultraviolet (UV) wavelengths (2–8). Foremost, multiple coherent pulses are required for many nonlinear X-ray spectroscopies. In addition, they would also enable linear schemes, such as time-domain X-ray interferometry (XRI) (7). Conceptually, these techniques are based on quantum interference of two photon fields with a variable time delay Δt and relative phase shift $\Delta\phi$. Spectral resolution is achieved by Fourier analysis and only limited by the maximum time delay at which interference is still measurable.

Generation of phase-locked, high-energy photon pulses has been proposed theoretically (9) and demonstrated in the extreme UV (8, 10). Here, we introduce an FEL operation mode, where high spectral resolution is obtained from phase-locked ultrafast X-ray (PHLUX) pulses, which can be delayed by up to 100 fs. The scheme is applicable in the soft and hard X-ray regime, does not require elaborate spectrometer design, and allows for tuning of acquisition efficiency versus energy resolution via the variable time delay and pulse duration. Compared to other schemes (*SI Appendix*), advantages are the availability of larger time delays, as well as tunability of the relative phase shift $\Delta\phi$ and amplitude of the pulses. This opens the door to coherent control and readout of prepared states, as well as the possibility of damage-free resonant X-ray scattering using π-shifted pulse pairs.

Generation of Phase-Locked X-Ray Pulses

Our approach to produce phase-locked pulses in the soft and hard X-ray regime is to overlay a fully coherent signal on an electron bunch that only lases in two well-defined longitudinal slices. It is achieved with a method (Fig. 1) that combines a "slotted" foil (11, 12) (or, equivalently, energy modulation or laser slicing, which may be more appropriate for high-repetition-rate FELs), transverse tilting of the electron beam (13–15), and self-seeding (16–20). The latter is a two-stage process to generate coherent X-ray pulses: The first FEL stage consists of a standard self-amplified spontaneous emission (SASE) section, whose output is spectrally filtered by a monochromator. This signal is

Significance

Brilliant, ultrashort, and coherent X-ray free-electron laser (FEL) pulses allow investigations of dynamics at the inherent time and length scale of atoms. However, missing are sequences of phase-locked X-ray pulses, desirable for time-domain correlation spectroscopies and coherent quantum control. Based on selective electron-bunch degradation in the accelerator, combined with two-stage, self-seeded photon emission, we propose an FEL mode, generating subfemtosecond, phase-locked X-ray pulse pairs with up to 100 fs delay. Splitting the electron bunch in the accelerator, instead of photon pulses in the beamline, avoids relative phase jitter. This enables time-domain interferometry, such as the X-ray analog of the ubiquitous Fourier transform infrared spectrometer, and, more generally, all of nonlinear and quantum optics requiring coherent copies of beams.

Author contributions: G.A. and S.G. designed research; S.R. and E.P. performed research; S.R. and E.P. analyzed data; and S.R., G.K., B.P., E.P., G.A., and S.G. wrote the paper.

Reviewers: J.H., SLAC National Accelerator Laboratory; and C.P., SLAC National Accelerator Laboratory.

Competing interest statement: J.H. and G.A., who have never had a joint research project, participated in a workshop that resulted in a report [B. Adams *et al.* arXiv [Preprint] (2019). https://arxiv.org/abs/1903.09317] co-authored by all participants and were co-authors of an invited perspective paper [J. B. Hastings, L. Rivkin, G. Aeppli, "Present and future accelerator-based X-ray sources: A perspective" in *The Future of Accelerators*, A. W. Chao, W. Chou, Eds. (2019), vol. 10, pp. 33–48] on accelerator-based light sources, which reported no original research. J.H. has served on advisory panels at the Paul Scherrer Institute, and G.A. has served on advisory panels at the SLAC National Accelerator Laboratory, where J.H. is employed. S.R. was a postdoctoral fellow and assistant/associate researcher of C. Pellegrini at the University of California Los Angeles from 2000 to 2008. S.G. was a postdoctoral fellow at Stanford University and SLAC from 2013 to 2015, which has led to one shared publication with J.H. [H. Jang *et al.*, Proc. Natl. Acad. Sci. U.S.A. **113**, 14645–14650 (2016)].

[1]To whom correspondence may be addressed. Email: aepplig@ethz.ch or simon.gerber@psi.ch.

This article contains supporting information online at https://www.pnas.org/lookup/suppl/doi:10.1073/pnas.2117906119/-/DCSupplemental.

Published February 9, 2022.

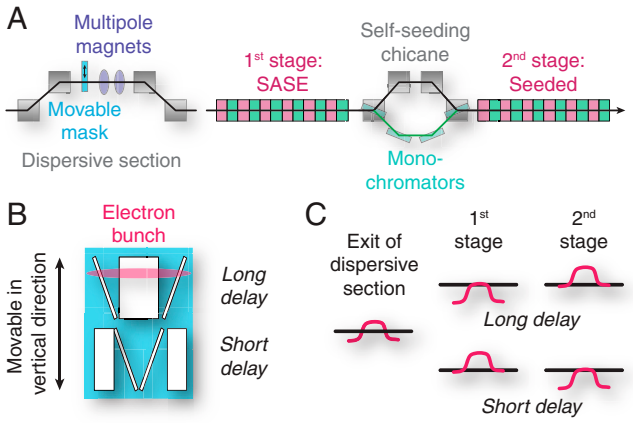

Fig. 1. (*A*) X-ray FEL beamline layout with a movable microfabricated mask (blue) and higher-order multipole magnets (purple) in a dispersive section, as well as the two undulator sections (pink–green) that are separated by a self-seeding chicane (gray–green). (*B*) The movable mask features a set of slots: One set preserves the electron bunch (pink) for SASE generation, whereas two narrow slits define the unspoiled parts of the electron bunch, from which the coherent signal originates. (*C*) The electron bunch is shaped with nonlinear transverse tilts using multipole magnets and realigned in the undulator section: For short (long) time delays, it is aligned on axis with the tails (central part) in the first and the central part (tails) in the second stage.

then used as a "seed" for the second stage and overlapped with the "sliced" parts of the electron bunch. In our method, the electron beam contains two parts defined by the slotted foil: One part is unspoiled, while the other part is spoiled, except for the two regions, as defined by the slits on a microfabricated mask (Fig. 1*B*). We separate the two regions transversely and correct the global beam trajectory such that one region is aligned to the SASE and the other region to the self-seeding stage. As a result, the first part drives the SASE section in saturation, while the two unspoiled slices in the second region amplify the seed signal to produce a phase-locked pulse pair.

The required spatial separation of the two regions is achieved by imposing a transverse tilt on the electron bunch in the dispersive section (see Fig. 1*C* and the start-to-end simulations in *SI Appendix*). Thereby, in both FEL stages, either the central part or the tails of the bunch is/are aligned to the undulator axis, whereas the respective other part undergoes betatron oscillations and does not contribute to the lasing process. The beam tilt is imposed where also the microfabricated mask is placed. Multipole magnets in the dispersive section can be used to alter the longitudinal and transverse position of the electron bunch, which is then preserved downstream. Namely, quadrupole magnets result in linear, sextupoles in quadratic, octupoles in cubic displacements, etc. A combination of a sextupole and a decapole magnet yields the desired step-function profile indicated in Fig. 1*C*. To switch between short and long time delays among the phase-locked pulses, the mask is moved vertically, and the alignment of the electron tilt is flipped.

Fig. 2 shows the performance of the PHLUX mode, in terms of radiation profile and spectrum, as well as phase stability, given the baseline capabilities of the SwissFEL Athos soft X-ray branch (21), assuming a seed energy of $E \sim 1{,}097$ eV and a self-seeding chicane with a resolving power of 50,000, foreseen as a future upgrade of the beamline. Here, the PHLUX mode is benchmarked in the soft X-ray regime, but the concept is equally applicable to hard X-rays. To create a phase-stable wave train, the bandwidth of the monochromators must be significantly smaller than the spectral width (inverse length) of individual SASE spikes (see discussion on self-seeding in *SI Appendix*). The modal structure in the spectrum depends on the temporal separation of the slices and, at the maximum $\Delta t_{\max} = 96$ fs considered here, corresponds to an energy resolution of $1/\Delta t_{\max} \sim 45$ meV, assuming Fourier-limited pulses; a smaller self-seeding resolving power, such as $\sim 5{,}000$ implemented at Linac Coherent Light Source (LCLS) (19), would still give a useful $\Delta t_{\max} \lesssim 20$ fs. A peak radiation power of ~ 2 GW results in a peak photon field strength of ~ 1 MV/cm at the source point. To reach nonlinear driving regimes, this field strength can be further increased; e.g., the baseline focusing capabilities of SwissFEL Athos allow for an increase by a factor of ~ 50 at the sample position.

The total width of the spectrum, i.e., the number of modes, depends on the slit width on the mask—wider slits result in narrower spectra. PHLUX delivers a minimal pulse separation of $\Delta t \sim 2$ fs, which is limited by the transverse size of the electron beam. In turn, it also determines the slit width of the mask, i.e., the minimal pulse duration. We note that 2 fs is the full-width at half-maximum (FWHM) of the electron slice, whereas lasing occurs mainly from the central portion, yielding a shorter photon pulse length of 0.5 fs FWHM. Our scheme is rather insensitive to the accuracy of the microfabrication process: Realistic tolerances, of order μm, result in pulse length changes of less than

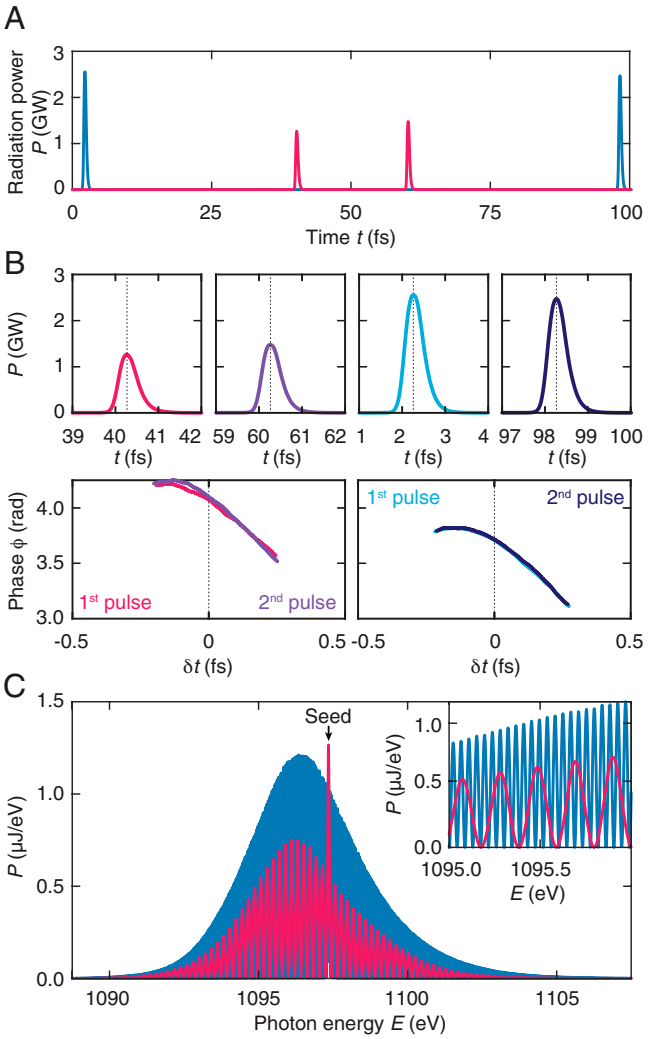

Fig. 2. (*A*) Radiation power profile of pulse pairs with a time delay of $\Delta t =$ 20 fs (pink) and 96 fs (blue) at a seed energy of $E \sim 1{,}097$ eV. (*B*) Close-up view of the radiation power *P* (*Upper*) and phase ϕ (*Lower*). Individual pulses have a duration of 0.5 fs FWHM. The phase is evaluated with respect to the central frequency of the seed. (*C*) Corresponding radiation power spectrum with tunable interference fringes, which can be exploited for spectroscopy.

100 as and have negligible effect on the phase and amplitude relation of the pulses.

Stability of Phase-Locked X-Ray Pulses

Because the two pulses follow a common path, the PHLUX scheme is fundamentally different and offers much higher phase stability than conventional X-ray split-and-delay approaches (22–24), where slight vibrations in the delaying monochromators and mirrors translate into phase jitter between the two pulses: For a central photon energy of $E \sim 1{,}097$ eV, $\Delta\phi = 1$ rad corresponds to a path-length difference of only ~ 1.8 Å. This translates into stability unachievable for standard setups, typically consisting of eight optical elements, which need to be set and held in place with respect to each other. In contrast, Fig. 2*B* shows that the peak-to-peak phase stability of PHLUX is always much better than $\Delta\phi \sim 60$ mrad. The absolute phase ϕ is not controllable, but, importantly, jitter in Δt and ϕ, determined by the mask stability and quality of the self-seeding monochromator, does not affect $\Delta\phi$ (see discussion on sources of beam jitter in *Materials and Methods*). That is, the FEL itself is used as a "perfect" beam splitter, which protects the phase difference $\Delta\phi$ from noticeable jitter. The clean, two-slit interference fringes in the radiation power spectrum (Fig. 2*C*), corresponding to the delay between pulses, attest to the quality of the pulse replication.

The phase stability of pulse pairs can be expressed by the first-order correlation function, generally defined as

$$g^{(1)}(t_1, t_2) = \frac{\langle E(t_1)E^*(t_2)\rangle}{\sqrt{\langle|E(t_1)|^2\rangle\langle|E(t_2)|^2\rangle}}.$$

$E(t)$ is the radiation field, which is evaluated at the times t_1 and $t_2 = t_1 + \Delta t$ of the peak of the first and second pulse, respectively. Δt is the pulse separation set by the machine parameters and the position of the slotted foil in the electron beam. Due to the phase rigidity of the individual pulses, there is no need for evaluation of a further time integral. An average is taken over many shots. To calculate $g^{(1)}$, we consider that the starting signal arises due to shot-noise of the incoherent spontaneous radiation from the electron beam. Importantly, neither SASE amplification nor the self-seeding monochromators change the white-noise characteristic of this starting signal (25). Therefore, the coherence properties are defined by the resolving power of the monochromators, and a Monte Carlo evaluation permits us to determine the coherence function $g^{(1)}(t_1, t_2)$. Amplification of two slices from the output field of the monochromators then inherits these coherence properties, unless the pulses are driven deep into saturation, which anyhow should be avoided, as it distorts the spectral quality of the FEL signal. Due to the nature of white noise, a fixed phase relation also results in a stable amplitude relation (26).

Fig. 3 illustrates the relative phase stability as a function of $\Delta t = t_2 - t_1$, reconstructed via $g^{(1)}(t_1, t_2)$. The signal degrades with increasing Δt, indicating the importance of a self-seeding chicane with highest possible resolving power. $g^{(1)} = 1$ means that the relative phase difference between two pulses is stable over many shots (coherent light), while for $g^{(1)} = 0$, the relative phase between pulses fluctuates randomly (chaotic light). A source for the reduced stability at large Δt could, in principle, be intrinsic shot noise fluctuations, which mainly affect the pulse phase at low seed power levels (~ 10 kW). However, this is not a concern for the parameters used here, when the electron bunch is driven close to saturation in the first FEL stage (MW seed power; see discussion on self-seeding in *SI Appendix*). On the other hand, we find rather tight, but nonetheless achievable, tolerances for electron beam parameters, such as the current, energy, energy spread, and transverse offset. All impact the gain length and, thereby, the phase from seeding to saturation. We note that this not only forms a limitation, but also provides a means to tune the phase and amplitude relation of the pulses (*Materials and Methods*).

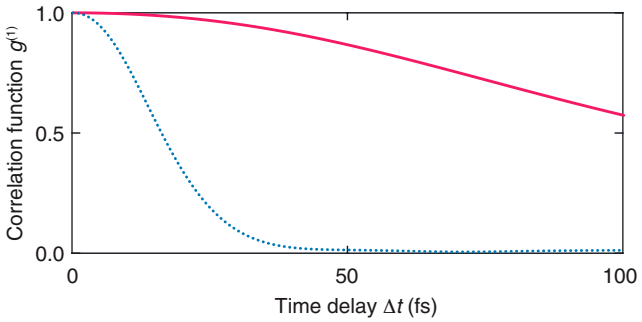

Fig. 3. Relative phase stability of the two X-ray pulses as a function of the time delay $\Delta t = t_2 - t_1$, benchmarked by the first-order correlation function $g^{(1)}(t_1, t_2)$. Pink and blue lines show the results assuming a self-seeding chicane with a resolving power of 50,000 and 10,000, respectively.

Time-Domain Interferometry

We turn now to the applications of our proposed X-ray beam splitter. The first is to take advantage of the power spectrum with tunable modulation and phase (Fig. 2*C*) to characterize absorption lines by their Fourier transforms without moving a monochromator. Spectroscopy can be performed by varying the phase shift and/or the delay between the pulses and collecting integrated counts on a detector (Fig. 4*A*). This technique is in complete analogy with Fourier transform infrared spectroscopy, where the incident beam is prepared in the spatial, rather than the time, domain by positioning a mirror. Such measurements—now in the X-ray regime—can underpin (optical) pump

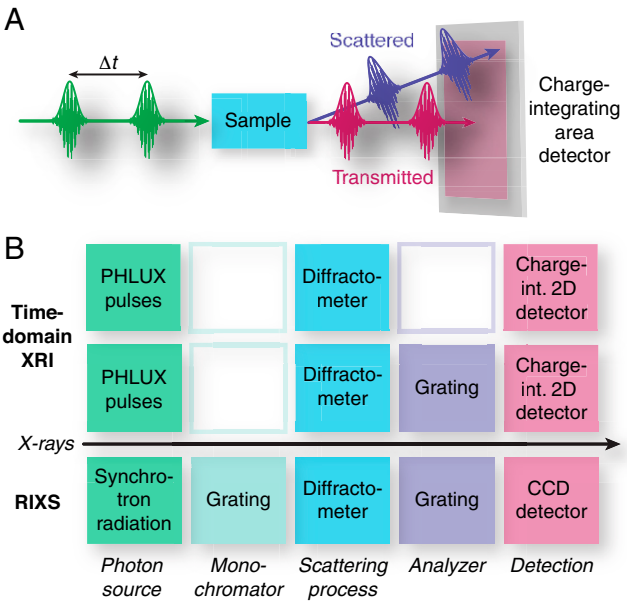

Fig. 4. (*A*) Schematic of time-domain XRI experiments where an incident pulse pair (green) with a fixed phase relation and time delay Δt is transmitted through (pink) or scattered by (purple) a sample. The respective signal is recorded on a two-dimensional (2D) charge-integrating (charge-int.) detector. (*B*) Frequency-domain RIXS requires high-resolution gratings before and after the sample for incident photon energy selection, analysis of the scattered signal and detection using an array of charge-coupled devices (CCD). Instead, XRI does not require a monochromator after the undulators and can benefit from the multiplexing in momentum transfers of an area detector.

(X-ray absorption)–probe experiments of, e.g., core-hole lifetimes modified via photo-excited modulation of states at the Fermi level. Judicious choices of Fourier components, where ΔE is specified by particular values of Δt, allow for highly efficient determinations of key parameters, such as the widths of well-defined lines.

Further possibilities exploiting the modulation illustrated in Fig. 2*C* and the presence of coherent processes in the sample include resonant scattering performed with and without an analyzer (Fig. 4*B*). The former enables resonant inelastic X-ray scattering (RIXS), where scans are performed by varying the incident beam modulation for fixed outgoing beam energies, rather than by moving a monochromator, and is complementary to RIXS instrument concepts, where the incident beam energy is encoded spatially on samples (27, 28). Benchmarking of frequency-domain RIXS against time-domain XRI shows that the latter can be a game changer at high-repetition rate X-ray FELs (*SI Appendix*).

Given that we are working with coherent beams on timescales comparable to core-hole lifetimes, it is interesting and important to consider that there is a similar timescale τ for the liberation of electrons from the cores of the atoms used for photodetection. This means, in a semiclassical description, that the detector measures not simply the integral over the square of the impinging time-dependent optical field $A(t)$, but rather the integral of the square of the convolution of $A(t)$ with a probability amplitude for the release of the electrons from the cores, which we take to decay exponentially as $e^{-t/\tau}$. The detector signal is then given by

$$I = \tau^{-2} \int \left| \int A(t') e^{(t-t')/\tau} \theta(t'-t) dt' \right|^2 dt,$$

where $\theta(t)$ is a Heaviside step function.

Our "beam splitter" produces optical fields, which can be regarded as sums of delta functions $\delta(t)$ in time, which can undergo stretching, scattering from or transmission through a sample. Whether or not such stretching occurs, the basic physics of what is measured by the detector is still captured by assuming $A(t) = A_1\delta(t) + A_2\delta(t-\Delta t)$, from which one obtains

$$I \propto |A_1|^2 + |A_2|^2 + 2\,\mathrm{Re}(A_1 A_2^*) e^{-\Delta t/\tau}.$$

The phase coherence of the pulse pairs guarantees that over timescales set by decoherence in the detector, i.e., $\tau \gtrsim \Delta t$, there will be visible interference terms, which measure directly the correlation between scattering amplitudes at different times for the sample. Thus, if we consider that the momentum transfer q is defined by the position of the relevant pixel on the detector (Fig. 4*A*), we are seeing the intermediate scattering functions $F(q,t)$ of the sample, which is proportional to the Fourier transform in space of the time-dependent, two-particle correlation functions $G(r,t)$ for generalized charge and/or magnetization densities.

On the other hand, for $\tau \ll \Delta t$, we will simply see the superposition of the ordinary scattering patterns, i.e., $I \propto |A_1|^2 + |A_2|^2$, and we can, by averaging over many pulse pairs, only measure the four-particle correlation function associated with speckle (29). The ergodic theorem tells us that speckle should rigorously vanish in the infinite volume limit for systems at equilibrium (26). However, the requirements for ergodicity are hardly met for many samples of contemporary interest, and our scheme will allow speckle correlations to be measured at unprecedentedly short times. We note, though, that minimal speckle represents an advantage for isolating the interference terms probing the two-particle correlation functions and for following these to $\Delta t > \tau$.

We turn now to what may well be the most far-reaching implication of phase-locked pairs of subfemtosecond X-ray pulses: the possibility of implementing the full program of quantum optics with X-rays. In particular, our scheme permits tuning of the phase difference and amplitudes of the two pulses (*Materials and Methods*), enabling coherent control and readout of prepared states, e.g., in photon-echo-type experiments, which at FELs have been demonstrated in the far-infrared (5, 30, 31) and extreme UV regime (8). The latter builds on a combination of phase-modulated seed pulses and high-gain harmonic generation, with which Ramsey fringes have been detected up to $E = 47.5$ eV. However, this approach cannot delay pulses less than $\Delta t \sim 150$ fs, which is long compared to the decoherence times τ for excitations of atomic cores (that is also relevant for the detector, as described above). In contrast, with the PHLUX scheme, pulses are "split" in the electron accelerator, which permits application at higher (soft and hard X-ray) energies and provides access to a larger momentum range. The addition of multiple evenly spaced slits on the microfabricated mask is an extension of the design shown in Fig. 1*B* and yields trains of phase-stable subfemtosecond pulses—an X-ray frequency comb.

Importantly, using our mode Δt can also be reduced to a few femtoseconds. In combination with the tunability of $\Delta\phi$, this allows for two few-femtosecond-delayed X-ray pulses with a phase difference of $\Delta\phi = \pi$. Beyond a critical threshold intensity, self-induced transparency occurs when short coherent light pulses interact with a dense medium, resulting in anomalously low absorption (32–34). Namely, this holds when, within an excitation cycle, the same amount of energy is coherently absorbed by a resonant two-level system, as is coherently emitted thereafter. For the single pulse experiments performed to date, scattering is eliminated along with absorption (35, 36). PHLUX enables generalizations of such experiments to pairs of π-shifted pulses, where the first pulse resonantly excites, and, shortly thereafter, the second pulse resonantly de-excites the sample. Such a sequence could take place on timescales faster than radiation damage and, nonetheless, would allow certain scattered signals to emerge. This would represent another potential route, in addition to ghost imaging (37), to damage-free X-ray scattering, with profound implications for all fields of X-ray science, particularly also for first-principle structure determination of solids and biological samples.

Materials and Methods

Simulations of the PHLUX mode were carried out with the three-dimensional, time-dependent FEL code Genesis 1.3 (38), currently released in its fourth version and available at http://genesis.web.psi.ch, using the parameters of the SwissFEL Athos soft X-ray beamline (21) at a seed photon energy of $E = 1{,}097$ eV. The input was prepared to model the emittance degradation from the mask and the seed signal. This also included variation of beam parameters for the slotted foil location to study the tolerances in the FEL performance. In addition, the particle tracker Elegant (39) was used to simulate the effect of the slotted foil on the electron bunch and the tilt with the higher-order multipole magnets in the dispersive section of the beamline. After the tracking with Elegant, the sliced beam parameters were analyzed to generate the corresponding input for the Genesis simulation.

Validation of Beam Dynamics Simulations. Genesis 1.3 (38) is one of the most commonly used codes for designing FEL facilities or to verify and interpret beam dynamics data. Since reproducing the results from the first hard X-ray lasing of LCLS (40), the code has been expanded to also include more advanced modeling, such as the recent echo-enabled harmonic generation experiment at the FERMI free-electron laser (41), which is extremely challenging due to the high harmonic conversion from 260 down to 4 nm. The simulation also agrees well with the performance of the SwissFEL Aramis hard X-ray beamline (42), all of which ensure our modeling capability of advanced operation modes, such as PHLUX.

Sources of Beam Jitter. We elaborate on the stability of the relative phase $\Delta\phi$ between the two pulses with respect to jitter in the electron-beam properties. Unlike conventional split-and-delay methods, jitter in the time separation between the two pulses affects the PHLUX operation mode less, since $\Delta\phi$ is given by the monochromator settings (*Tuning of the Phase Difference and Radiation Power*), as well as the electron-bunch phase space portrait going into the undulators after the initial seeding stage.

Also, FEL amplification of the two sliced pulses enhances the amplitude of the radiation by several orders of amplitude, but changes the radiation phase of the seed only very little. Therefore, interference of the two pulses remains constructive at the central wavelength of the seed signal. Only the modulation within the envelope of the power spectrum (Fig. 2 *C*, *Inset*) varies with jitter, but the central line remains unchanged. Moreover, there is also only a weak phase variation if the growth rate of the FEL amplification process between the two slice changes from shot to shot. Since global jitter, such as that of the electron-beam mean energy, affects both slices equally, the phase relation between the two FEL pulses remains unchanged, and, therefore, the stability of the central frequency in the interference spectrum is preserved. Only relative beam parameter jitter has an effect on $\Delta\phi$. Here, the strongest contribution arises from the shot-to-shot fluctuation in the electron-beam parameters due to the micro-bunch instability. In seeded FELs, this becomes apparent in the so-called pedestal of the spectra (18, 19, 43). For our application, this results in a loss of coherence between the two pulses (damping of first-order correlation function $g^{(1)}(t_1, t_2)$ shown in Fig. 3). The micro-bunching instability is difficult to simulate, but its impact on the performance of PHLUX scheme can be estimated from varying the beam parameters. *SI Appendix*, Fig. S1 shows this dependence of the radiation power and phase relation on the most important sources of jitter. At the SwissFEL Athos beamline, we expect that the relative peak current and energy spread will vary by less than 1% and, thus, do not significantly contribute to jitter between the two pulses. Concerning the relative mean energy and trajectory jitter, the standard requirements to operate self-seeding, e.g., $< 10^{-4}$ mean energy and < 10 μm orbit stability, already imply acceptable phase and power jitter between the two pulses. These estimates are based on the assumption of an optimally configured laser heater (44), which minimizes the impact of the microbunching instability.

Tuning of the Phase Difference and Radiation Power. The relative phase difference $\Delta\phi$ between the two X-ray pulses can be controlled by a slight detuning of the self-seeding monochromator: If the beam energy, undulator field, and central wavelength of the self-seeding monochromator are identical, then the phase along the seed pulse is constant. Detuning of the latter induces a linear spatial change of the seed pulse phase. Consequently, also the sliced portions of the pulse then feature a phase difference given by

$$\Delta\phi = (k_{\mathrm{MC}} - k_{\mathrm{R}})c\Delta t,$$

where c is the speed of light. k_{MC} and k_{R} are the central wavenumbers for the self-seeding monochromator and radiator, respectively. For example, a seed photon energy of $E = 1{,}097$ eV and time delay of $\Delta t = 7$ fs requires a relative detuning of 2.7×10^{-4} for a pulse-to-pulse phase difference of $\Delta\phi = \pi$. Such manipulation is difficult for pulse pairs that overlap in time, but else this variant of the PHLUX scheme does not represent a major restriction in terms of operation.

The total radiation power is tunable by use of a so-called laser heater (44) or by removing/adding undulator modules that contribute to the lasing process. The relative amplitude or rather radiation power ΔP of the two pulses can then be varied by, for example, adding a transverse or energy chirp to the beam. That way, the radiation power of the two phase-locked pulses can be individually adjusted, e.g., for Ramsey ($\pi/2$ -$\pi/2$) or Hahn-echo ($\pi/2$ -π) type experiments.

Data Availability. All study data are included in the article and/or supporting information.

Note Added in Proof. In the course of the review process, we became aware of the recent demonstration of phase-stable hard X-ray pulse pairs based on superfluorescence and seeded stimulated emission (45), which underlines the importance of the more general working principle, and experiments enabled thereby, reported here (46).

ACKNOWLEDGMENTS. We acknowledge fruitful discussions with A. Cavalieri, R. Follath, G. Matmon, L. Patthey, B. Schmitt, T. Schmitt, and V. N. Strocov. This project received funding from the European Research Council under the European Union's Horizon 2020 research and innovation program, within the Hidden, Entangled and Resonating Order (HERO) project with Grant Agreement 810451. G.K. was supported by Swiss National Science Foundation Contract 165550.

1. E. A. Seddon *et al.*, Short-wavelength free-electron laser sources and science: A review. *Rep. Prog. Phys.* **80**, 115901 (2017).
2. N. F. Ramsey, A molecular beam resonance method with separated oscillating fields. *Phys. Rev.* **78**, 695–699 (1950).
3. S. Mukamel, *Principles of Nonlinear Optical Spectroscopy* (Cambridge University Press, Cambridge, UK, 1995).
4. S. T. Cundiff, J. Ye, Femtosecond optical frequency combs. *Rev. Mod. Phys.* **75**, 325–342 (2003).
5. P. T. Greenland *et al.*, Coherent control of Rydberg states in silicon. *Nature* **465**, 1057–1061 (2010).
6. T. Kampfrath, K. Tanaka, K. A. Nelson, Resonant and nonresonant control over matter and light by intense terahertz transients. *Nat. Photonics* **9**, 680–690 (2013).
7. S. Chatterjee, T. Nakajima, Ramsey interferometry for resonant Auger decay through core-excited states. *Phys. Rev. A* **94**, 023417 (2016).
8. A. Wituschek *et al.*, Tracking attosecond electronic coherences using phase-manipulated extreme ultraviolet pulses. *Nat. Commun.* **11**, 883 (2020).
9. N. R. Thompson, B. W. J. McNeil, Mode locking in a free-electron laser amplifier. *Phys. Rev. Lett.* **100**, 203901 (2008).
10. D. Gauthier *et al.*, Generation of phase-locked pulses from a seeded free-electron laser. *Phys. Rev. Lett.* **116**, 024801 (2016).
11. P. Emma *et al.*, Femtosecond and subfemtosecond X-ray pulses from a self-amplified spontaneous-emission-based free-electron laser. *Phys. Rev. Lett.* **92**, 074801 (2004).
12. Y. Ding *et al.*, Generating femtosecond X-ray pulses using an emittance-spoiling foil in free-electron lasers. *Appl. Phys. Lett.* **107**, 191104 (2015).
13. M. W. Guetg, B. Beutner, E. Prat, S. Reiche, Optimization of free electron laser performance by dispersion-based beam-tilt correction. *Phys. Rev. Spec. Top. Accel. Beams* **18**, 030701 (2015).
14. M. W. Guetg, A. A. Lutman, Y. Ding, T. J. Maxwell, Z. Huang, Dispersion-based fresh-slice scheme for free-electron lasers. *Phys. Rev. Lett.* **120**, 264802 (2018).
15. P. Dijkstal, A. Malyzhenkov, S. Reiche, E. Prat, Demonstration of two-color X-ray free-electron laser pulses with a sextupole magnet. *Phys. Rev. Accel. Beams* **23**, 030703 (2020).
16. J. Feldhaus, E. L. Saldin, J. R. Schneider, E. A. Schneidmiller, M. V. Yurkov, Possible application of X-ray optical elements for reducing the spectral bandwidth of an X-ray SASE FEL. *Opt. Commun.* **140**, 341–352 (1997).
17. E. L. Saldin, E. A. Schneidmiller, Y. V. Shvyd'ko, M. V. Yurkov, X-ray FEL with a meV bandwidth. *AIP Conf. Proc.* **581**, 153 (2001).
18. J. Amann *et al.*, Demonstration of self-seeding in a hard-X-ray free-electron laser. *Nat. Photonics* **6**, 693–698 (2012).
19. D. Ratner *et al.*, Experimental demonstration of a soft X-ray self-seeded free-electron laser. *Phys. Rev. Lett.* **114**, 054801 (2015).
20. C. Emma *et al.*, Experimental demonstration of fresh bunch self-seeding in an X-ray free electron laser. *Appl. Phys. Lett.* **100**, 154101 (2017).
21. R. Abela *et al.*, The SwissFEL soft X-ray free-electron laser beamline: Athos. *J. Synchrotron Radiat.* **26**, 1073–1084 (2019).
22. T. Osaka *et al.*, Characterization of temporal coherence of hard X-ray free-electron laser pulses with single-shot interferograms. *IUCrJ* **4**, 728–733 (2017).
23. D. Zhu *et al.*, Development of a hard X-ray split-delay system at the Linac Coherent Light Source. *Proc. SPIE* **10237**, 102370R (2017).
24. W. Lu *et al.*, Development of a hard X-ray split-and-delay line and performance simulations for two-color pump-probe experiments at the European XFEL. *Rev. Sci. Instrum.* **89**, 063121 (2018).
25. E. L. Saldin, E. V. Schneidmiller, M. V. Yurkov, *The Physics of Free Electron Lasers* (Springer-Verlag, Berlin, 2000).
26. J. W. Goodman, *Statistical Optics* (Wiley, Hoboken, NJ, 2015).
27. V. N. Strocov, Concept of a spectrometer for resonant inelastic X-ray scattering with parallel detection in incoming and outgoing photon energies. *J. Synchrotron Radiat.* **17**, 103–106 (2010).
28. K. J. Zhou, S. Matsuyama, V. N. Strocov, hv^2-concept breaks the photon-count limit of RIXS instrumentation. *J. Synchrotron Radiat.* **27**, 1235–1239 (2020).
29. G. Grübel, G. B. Stephenson, C. Gutt, H. Sinn, T. Tschentscher, XPCS at the European X-ray free electron laser facility. *Nucl. Instrum. Methods Phys. Res. B* **262**, 357–367 (2007).
30. K. L. Litvinenko *et al.*, Coherent creation and destruction of orbital wavepackets in Si:P with electrical and optical read-out. *Nat. Commun.* **6**, 6549 (2015).
31. S. Chick *et al.*, Coherent superpositions of three states for phosphorous donors in silicon prepared using THz radiation. *Nat. Commun.* **8**, 16038 (2017).
32. S. L. McCall, E. L. Hahn, Self-induced transparency by pulsed coherent light. *Phys. Rev. Lett.* **18**, 908–911 (1967).
33. S. L. McCall, E. L. Hahn, Self-induced transparency. *Phys. Rev.* **183**, 457–485 (1969).
34. J. Stöhr, A. Scherz, Creation of X-ray transparency of matter by stimulated elastic forward scattering. *Phys. Rev. Lett.* **116**, 019902 (2016).
35. B. Wu *et al.*, Elimination of X-ray diffraction through stimulated X-ray transmission. *Phys. Rev. Lett.* **117**, 027401 (2016).
36. Z. Chen *et al.*, Ultrafast self-induced X-ray transparency and loss of magnetic diffraction. *Phys. Rev. Lett.* **121**, 137403 (2018).
37. Z. Li, N. Medvedev, H. N. Chapman, Y. Shih, Radiation damage free ghost diffraction with atomic resolution. *J. Phys. At. Mol. Opt. Phys.* **51**, 025503 (2017).
38. S. Reiche, GENESIS 1.3: A fully 3D time-dependent FEL simulation code. *Nucl. Instrum. Methods Phys. Res. A* **429**, 243–248 (1999).
39. M. Borland, "Elegant: A flexible sdds-compliant code for accelerator simulation" (Tech. Rep. LS-287, Advanced Photon Source, Lemont, IL, 2000).
40. P. Emma *et al.*, First lasing and operation of an ångstrom-wavelength free-electron laser. *Nat. Photonics* **4**, 641–647 (2010).
41. P. R. Ribič *et al.*, Coherent soft X-ray pulses from an echo-enabled harmonic generation free-electron laser. *Nat. Photonics* **13**, 555–561 (2019).
42. E. Prat *et al.*, A compact and cost-effective hard X-ray free-electron laser driven by a high-brightness and low-energy electron beam. *Nat. Photonics* **14**, 748–754 (2020).
43. I. Nam *et al.*, High-brightness self-seeded X-ray free-electron laser covering the 3.5 keV to 14.6 keV range. *Nat. Photonics* **15**, 435–441 (2021).
44. Z. Huang *et al.*, Measurements of the Linac Coherent Light Source laser heater and its impact on the X-ray free-electron laser performance. *Phys. Rev. Spec. Top. Accel. Beams* **13**, 020703 (2010).
45. Y. Zhang *et al.*, Generation of intense phase-stable femtosecond hard X-ray pulse pairs. arXiv [Preprint] (2021). https://arxiv.org/abs/2110.08262 (Accessed 29 December 2021).
46. S. Reiche *et al.*, Towards the perfect X-ray beam splitter. arXiv [Preprint] (2020). https://arxiv.org/abs/2010.00230 (Accessed 29 December 2021).